The Astrophysical Journal, 980:73 (14pp), 2025 February 10 https://doi.org/10.3847/1538-4357/ada55f


# Unraveling the Kinematic and Morphological Evolution of the Small Magellanic Cloud

S. R. Dhanush[1,2], A. Subramaniam[1], and S. Subramanian[1]
[1] Indian Institute of Astrophysics, Bangalore, 560034, India; srdhanushsr@gmail.com
[2] Pondicherry University, R.V. Nagar, Kalapet, Puducherry, 605014, India
*Received 2024 October 22; revised 2024 December 23; accepted 2024 December 31; published 2025 February 5*

## Abstract

We model the kinematics of the Small Magellanic Cloud (SMC) by analyzing the proper motions (PMs) from Gaia DR3 of nine different stellar populations, including young main-sequence (MS) stars (<2 Gyr), red giant branch stars, red clump stars, red giants with line-of-sight velocities, and three groups of star clusters. This analysis is carried out using a robust Markov Chain Monte Carlo method, to derive up to seven kinematic parameters. We trace the evolution from a nonrotating flattened elliptical system, as mapped by the old population, to a rotating highly stretched disk structure, as denoted by the young MS stars and clusters (<400 Myr). We estimate that the inclination $i$ (∼58°–82°) decreases and the position angle $\Theta$ (∼180°–240°) increases with age. We estimate an asymptotic velocity of ∼49–89 km s$^{-1}$ with a scale radius of ∼6–9 kpc for the young MS populations, with velocity dispersion of ∼11 km s$^{-1}$, suggesting a rotation-supported disk structure. Our models estimate a line-of-sight extension of ∼30 kpc, in agreement with observations. We identify four regions of the SMC showing anomalies in the residual PM: the East Anomaly, the Southeast Anomaly (SEA), the South Anomaly, and the West Anomaly. The SEA appears like an infalling feature and is identified for the first time. The tidal imprints observed in the residual PM of the SMC suggest that its evolution is considerably shaped by the recent interaction with the Large Magellanic Cloud.

*Unified Astronomy Thesaurus concepts:* Small Magellanic Cloud (1468); Dwarf galaxies (416); Star clusters (1567); Tidal interaction (1699)

## 1. Introduction

The Magellanic Clouds (MCs) consist of two irregular dwarf galaxies in the Local Group, the Large Magellanic Cloud (LMC) and the Small Magellanic Cloud (SMC). The LMC and the SMC are located at a distance of 49.59 ± 0.09 kpc (G. Pietrzyński et al. 2019) and 62.44 ± 0.47 kpc (D. Graczyk et al. 2020), respectively. The interactions between the MCs have resulted in the formation of a few unique features in this system. The Magellanic system consists of the MCs along with the Magellanic Stream, a trail of neutral hydrogen that spans more than 100° in the sky (M. E. Putman et al. 2003; D. L. Nidever & S. R. Majewski 2008; E. D'Onghia & A. J. Fox 2016), the Magellanic Bridge, which features both stellar and gaseous components (L. T. Gardiner et al. 1994; E. Muller & K. Bekki 2007), and the Leading Arm, another gaseous stream with multiple filaments (M. E. Putman et al. 1998; M. S. Venzmer et al. 2012). However, the evolution of the MCs is influenced not only by their mutual interactions but also by their interactions with the Milky Way (M. D. Weinberg 2000; J. D. Diaz & K. Bekki 2012; F. Hammer et al. 2015).

Significant efforts have been made to understand the structure of the SMC. The galaxy is traditionally thought to be a spheroidal or ellipsoidal 3D system, and the overall feature of the SMC is governed by its intrinsic hydrodynamics rather than tidal interactions (D. Zaritsky et al. 2000). According to M. R. L. Cioni et al. (2000), younger stars in the SMC display an irregular structure characterized by spiral arms and tidal features. In contrast, studies of the older population indicate that they are distributed in a spherical or ellipsoidal manner (S. Subramanian & A. Subramaniam 2012—hereafter, S12; S. Deb et al. 2015; S. Rubele et al. 2018—hereafter, R18; D. El Youssoufi et al. 2019—hereafter, Y19). Studies by R. Haschke et al. (2012), S. Subramanian & A. Subramaniam (2015; hereafter, S15), and E. M. DiTeodoro et al. (2018; hereafter, D18) have suggested that the SMC can have a disk morphology as well. S. Deb et al. (2019) showed that the northeastern part of the SMC bar is closer to us than the southwestern part. The bar is notably more pronounced in the youngest main-sequence (MS) stars of the SMC and appears fragmented, potentially as a result of tidal interactions (Y19).

The estimated line-of-sight (LOS) depth of the SMC is found to be greater than that of the LMC and reaches more than ∼20 kpc (S12; A. M. Jacyszyn-Dobrzeniecka et al. 2016—hereafter, J16, 2017; T. Muraveva et al. 2018; V. Ripepi et al. 2017—hereafter, R17). The studies of the red clump (RC) population have shown a distance bimodality in the SMC as well, suggesting that an eastern foreground stellar population is situated more than ∼10 kpc in front of the main body of the SMC (D. L. Nidever et al. 2010; S. Subramanian et al. 2017; D. El Youssoufi et al. 2021; A. O. Omkumar et al. 2021; D. James et al. 2021). Recently, J. D. Sakowska et al. (2024) have reported that the northeastern region of the SMC has an LOS depth of ∼7 kpc.

Over the past decade, several kinematic studies and models of the SMC have been conducted (E. Costa et al. 2011—hereafter, C11; N. Kallivayalil et al. 2013—hereafter, K13; R. P. van der Marel & J. Sahlmann 2016—hereafter, V16; P. Zivick et al. 2018—hereafter, Z18; Gaia Collaboration et al. 2018—hereafter, G18; M. DeLeo et al. 2020—hereafter, D20; F. Niederhofer et al. 2021—hereafter, N21). Also, it has been observed that the HI gas of the SMC exhibits considerable internal rotation (S. Stanimirović et al. 2004—hereafter, S04; D18), while the older population has a weak or little rotation

(J. Harris & D. Zaritsky 2006; Z18; P. Zivick et al. 2021—hereafter, Z21). The young stars show an ordered motion toward the Magellanic Bridge, with a larger proper motion (PM) than that of the main body of the SMC (M. S. Oey et al. 2018).

Previous studies indicate that the distribution of younger and older populations within the SMC differs significantly. Additionally, the morphology and kinematics of the SMC vary, depending on the specific tracer population used in the study. Moreover, many earlier studies do not adequately address the estimated LOS depth using a model. To comprehend the substantial LOS depth, morphology, and structure of the SMC, it is essential to model the kinematics of the galaxy as a function of different populations (both young and old). In our study, we address these aspects by presenting a 2D model of the SMC that incorporates various populations, both young and old, utilizing data from Gaia DR3. Additionally, we develop a 3D model of the SMC using Red Giants that have LOS velocity ($v_{\rm los}$) information as well.

In this study, we aim to achieve the following: (1) to develop a base kinematic disk model of the SMC that aligns with the observed kinematics of both young and old stars in the galaxy; (2) to detect the signals of rotation in the SMC, based on the age of the stellar population; (3) to estimate the kinematic disk parameters, which aid in revealing the orientation, galaxy plane morphology, and LOS features of the SMC; and (4) to investigate the tidal interaction/influence on the SMC by the LMC, based on the kinematic response of both the young and old populations. Addressing these points will offer insights into the structural and kinematic evolution of the SMC within the Magellanic system.

The paper is arranged as follows. In Section 2, we describe the data sets used for our modeling. In Section 3, we describe the procedures of our kinematic model. In Section 4, we present the estimated kinematic parameters of our data sets, followed by the estimation of the residual PM. The discussions based on our results are presented in Section 5, followed by Section 6, which summarizes our work.

## 2. Data

To model the young and old populations of the SMC, we use the cleaned SMC Gaia DR3 catalog provided in the study by Ó. Jiménez-Arranz et al. (2023—hereafter, J23), which is produced based on a robust neural network classifier. We retained the sources with probability $P \geqslant 0.31$ for optimal selection of the SMC sources, as recommended by the authors. We selected the SMC sources within a box of $7\overset{\circ}{.}5$, centered on the SMC. We adopted the optical center of the SMC ($\alpha_0 = 13\overset{\circ}{.}05$ and $\delta_0 = -72\overset{\circ}{.}83$; G. de Vaucouleurs & K. Freeman 1972) in our modeling. We then classified the SMC sources into subsamples: Young MS 1 (YMS1; ages <50 Myr), Young MS 2 (YMS2; 50 < ages < 400), Young MS 3 (YMS3; mixed ages reaching up 1–2 Gyr), and red giant branch (RGB), based on the polygon selections in the color–magnitude diagram (CMD) of the SMC as provided in Section 2.3.2 of Gaia Collaboration et al. (2021—hereafter, G21). We also selected the RC population from the CMD based on the selection criterion mentioned in S. Saroon & S. Subramanian (2022). The selected subsamples are highlighted and displayed on the CMD, as shown in Figure 1. Since these data sets lack LOS velocity information, we crossmatched the J23 catalog with the Red Giants catalog by P. D. Dobbie et al. (2014—hereafter, D14) and found 3545 stars, which have LOS velocity information as well.

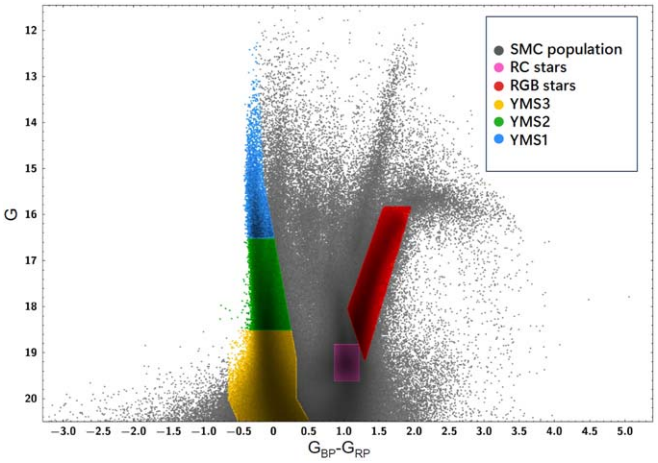


**Figure 1.** The CMD illustrating the selection of various stellar populations in the SMC as defined in Section 2 is presented here. The populations are highlighted in corresponding colors: RC stars (pink), RGB stars (red), YMS3 (yellow), YMS2 (green), and YMS1 (light blue).

We also used the data set of 280 star clusters in the SMC from the analysis of S. R. Dhanush et al. (2024a—hereafter, D24), spanning ages from ∼12 Myr to 3.4 Gyr, which used Gaia DR3 to estimate the age, metallicity, extinction, and distance modulus. The clusters were parameterized after field star decontamination, as explained in Section 2 of D24. The clusters were divided into three age groups: (1) young clusters (CLSY—ages <400 Myr; 143 clusters), (2) intermediate-age clusters (CLSI—400 Myr < ages <1 Gyr; 65 clusters), and (3) old clusters (CLSO—ages >1 Gyr; 72 clusters).

The sources shown in Figure 1 are then orthographically projected with the SMC center, using the equations outlined in G21. We use a bin size of $0\overset{\circ}{.}25$ to bin the sources and calculate the median PM and the corresponding standard errors for each bin. We retain bins with more than five stars, resulting in 140 YMS1, 372 YMS2, 1093 YMS3, 1288 RGB, and 1731 RC bins as the final data sets for the modeling. The bin size and minimum number of stars per bin are determined through multiple trials with different bin sizes and star counts. The optimal combination is selected based on the visual clarity of the features observed in the vector point diagram of the bulk PM and residual PM (see Section 4). The radial coverage of the Red Giants from D14 is mostly within ∼3° of the SMC, so we model them as individual sources rather than binning the data. For clusters, we calculate the median PM and the associated standard error of the stars within each cluster.

The data sets mentioned above are used for modeling the SMC. The following section provides the analytical background and the modeling procedure.

## 3. Kinematic Model of the SMC

The following sections offer an overview of the theoretical framework used in our modeling, as well as the Bayesian methodology employed to estimate the optimal kinematic parameters for the nine data sets.

### 3.1. Analytical Background of the Modeling

We perform the kinematic modeling of the SMC based on the equations outlined by R. P. van der Marel et al. (2002—hereafter, V02). The method involves defining the directional vectors of the local PMs of sources in the west and north ($M_{\rm W}$, $M_{\rm N}$) in the sky plane, using a series of several independent model parameters. The parameters selected for our model encompass the inclination of the SMC disk ($i$), the position angle of the line of nodes measured from the west ($\theta$), the amplitude of the tangential velocity of the SMC's center of mass (COM; $v_t$), the tangential angle made by $v_t$ ($\theta_t$), the scale radius ($R_f$), the asymptotic velocity ($v_f$), and the systemic velocity ($v_{\rm sys}$). Our modeling process is aimed at determining the best-fitting values for these kinematic parameters. It should be noted that the disk we expect to trace is the projected distribution of the ellipsoidal SMC along its semimajor and semiminor axes.

We assume that the PMs of the sources in the SMC include both the COM motion and rotational components within the disk model. We use the parametric equation for rotation as described in D18 and also assume that the SMC disk experiences no precession or nutation.

The following section describes the modeling procedure employed to estimate the best-fitting kinematic parameters for the data sets discussed in Section 2.

### 3.2. Modeling Procedure

The best-fitting kinematic parameters of the SMC are estimated using the Markov Chain Monte Carlo (MCMC) serial-stretch-move sampling algorithm introduced by J. Goodman & J. Weare (2010). The implementation of MCMC is similar to the previous study by S. R. Dhanush et al. (2024b) on the kinematic model of the LMC. The model PM ($\mu_{\rm W,m}$, $\mu_{\rm N,m}$) and the observed PM ($\mu_{\rm W,o}$, $\mu_{\rm N,o}$) are used to construct the log-likelihood function ($\ln\mathcal{L}$), which can be used with the associated west and north direction standard errors of the observed data sets ($\sigma_{\rm W,o}$,$\sigma_{\rm N,o}$), to sample the best-fitting parameter with MCMC. For Red Giants with observed LOS velocities ($v_{\rm los,o}$) and associated errors ($\sigma_{\rm los,o}$), we include the model LOS velocity ($v_{\rm los,m}$) in the $\ln\mathcal{L}$ as well. The equation for $\ln\mathcal{L}$ is given by

$$\ln\mathcal{L} = -0.5\sum_{i=1}^{n}\Bigg[\ln(2\pi\sigma^2_{\rm W,o,}{}_i) + \frac{(\mu_{\rm W,o,}{}_i - \mu_{\rm W,}{}_{m,i})^2}{\sigma^2_{\rm W,o,}{}_i} + \ln(2\pi\sigma^2_{N,\rm o,}{}_i) + \frac{(\mu_{N,\rm o,}{}_i - \mu_{N,}{}_{m,i})^2}{\sigma^2_{N,\rm o,}{}_i} + \ln(2\pi\sigma^2_{\rm los,o,}{}_i) + \frac{(v_{\rm los,o,}{}_i - v_{\rm los,}{}_{m,i})^2}{\sigma^2_{\rm los,o,}{}_i}\Bigg]. \quad (1)$$

It is to be noted that the last two terms in Equation (1) are excluded for the eight data sets that lack $v_{\rm los}$ information. Additionally, we consider two primary variants of the model: one that includes the rotation component of the observed PMs and one that does not. Both variants are tested across each data set to determine which best represents the different stellar populations of the SMC. The final model for each population is chosen based on the variant (with or without rotation) that shows convergence in the posterior distribution of the sampled parameters. For data sets lacking $v_{\rm los,o}$, the $v_{\rm sys}$ is fixed at 145.6 km s$^{-1}$ (V02), but it is treated as a free parameter otherwise. The kinematic center is fixed at $\alpha_0 = 13.^{\circ}05$ and $\delta_0 = -72.^{\circ}83$, which is the optical center adopted for selecting the coverage of the SMC in this study (Section 2). The priors for $i$, $\theta$, $v_t$, and $v_f$ are uniformly chosen, while $R_f$ is assigned a Gaussian prior centered at 1.1 kpc (D18) with an extended $3\sigma$ range to effectively explore the parameter space.

We executed 2000 steps of MCMC iteration involving 200 walkers evolving sequentially at each step. From the sampled posterior values for the parameters, we focused on the final 50%, calculating their median alongside the 16th and 84th percentile errors for parameter estimation. In the following section, we present the results obtained from the above modeling procedures.

## 4. Results

In this study, we present a 2D kinematic model of the SMC by analyzing various SMC populations using Gaia DR3 data. These populations include YMS1, YMS2, YMS3, RC, RGB, CLSY, CLSI, and CLSO. The study covers a radius within $\sim 7.^{\circ}5$ from the SMC center. Additionally, we develop a 3D disk model of the SMC using the Red Giants and their LOS velocities estimated by D14. The modeling indicates that rotation in the SMC is present in YMS1, YMS2, CLSY, and CLSI. In contrast, CLSO, YMS3, RGB, RC, and Red Giants with $v_{\rm los}$ in the SMC show no evidence of significant rotation. Figure 2 shows the sampled posterior distribution of the kinematic parameters for YMS1. Figure 3 presents a comparison of the sampled posterior distributions of the kinematic parameters for the RGB population without $v_{\rm los}$ and the Red Giants with $v_{\rm los}$. The best-fitting kinematic parameters for all the data sets considered in this study are tabulated in Table 1.

In the following sections, we detail the results from our models corresponding to different SMC populations. We highlight some notable features in each population and also present the residual PM map and its distribution.

### 4.1. YMS1 and YMS2

The observed bulk PMs of YMS1 and YMS2 in the sky plane are shown in Figures 4(a) and (d), respectively. We find these populations support rotation components in their bulk PMs. However, we estimate a larger $v_f$ and $R_f$ for YMS1 ($\sim$89 km s$^{-1}$ and 9 kpc, respectively) compared to the YMS2 population ($\sim$49 km s$^{-1}$ and 6 kpc, respectively). Meanwhile, the estimated COM PM values in the west and north directions ($\mu_{\rm W,com}$, $\mu_{\rm N,com}$) for YMS1 ($-0.657 \pm 0.008$, $-1.262 \pm 0.007$) and YMS2 ($-0.712 \pm 0.010$, $-1.283 \pm 0.010$) do not show any significant deviation. The estimated $i$ shows an offset of $4.^{\circ}26 \pm 1.^{\circ}13$, while the position angle of the line of nodes, measured from north $\Theta$ ($\theta - 90°$), does not show any significant variation.

Figures 4(b) and (e) depict the residual PMs (observed PM – model PM) for YMS1 and YMS2, respectively. We visually detect four anomalies in the residual PM map of YMS2 by identifying large deviations in the amplitude and direction of the residual vectors. These include the East Anomaly (EA), which is significant beyond $\sim 2°$ with the residual PM directed toward the east and northeast; the Southeast Anomaly (SEA), located in the southeast and extending beyond $\sim 4°$, where the residual PM is directed toward the south with an indication of counter-rotation; the South Anomaly (SA), found in the southern region beyond $\sim 1°$, where the residual PM is directed

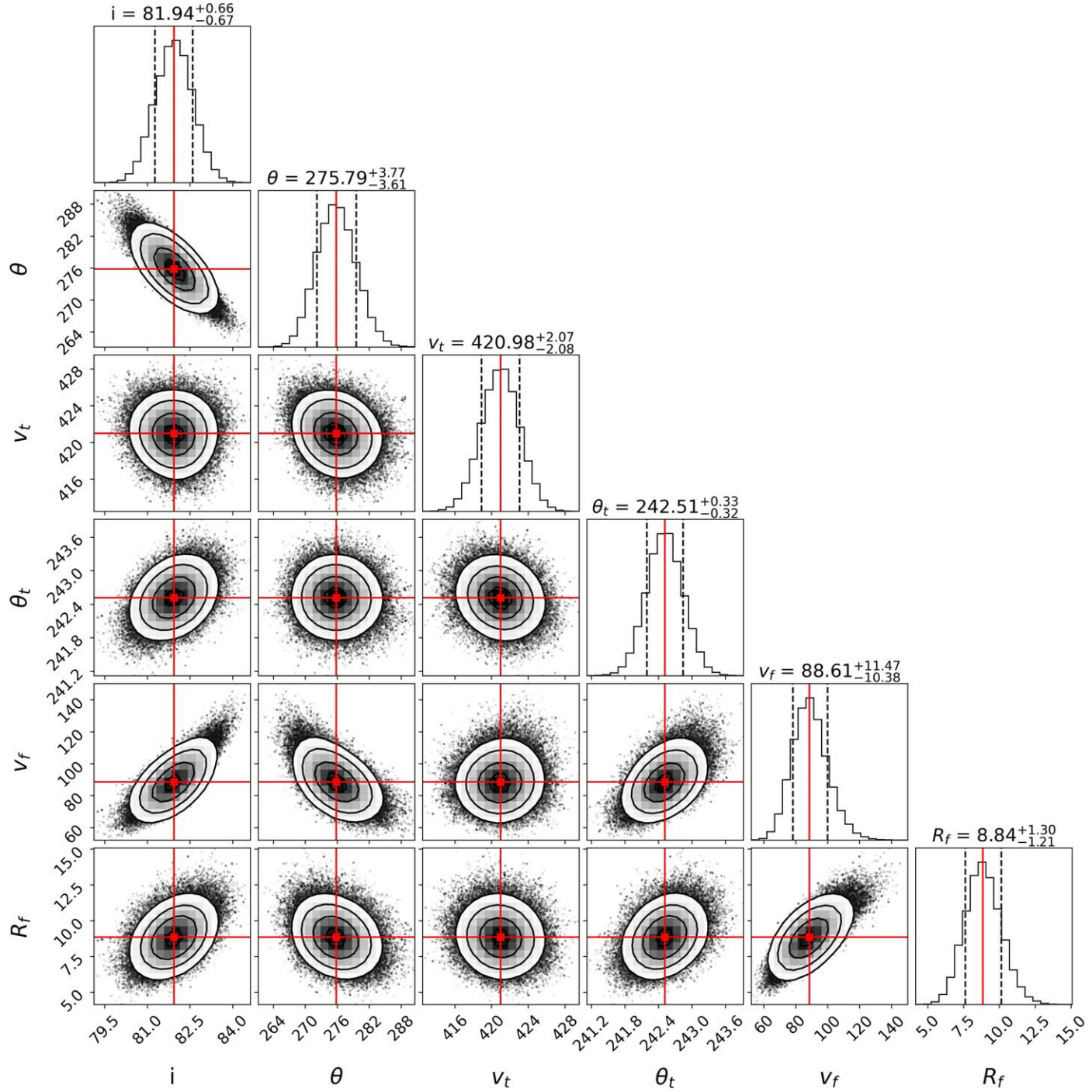


**Figure 2.** The corner plot representing the sampled posterior distribution of kinematic parameters for YMS1 is shown here. The vertical red lines represent the median values, and the black dashed lines represent the 16th and 84th percentiles.

toward the southeast; and the more prominent West Anomaly (WA), which extends from the central regions of the SMC to the southwest, with the residual PM directed westward. YMS1 exhibits significantly less pronounced SEA, WA, and SA, though the EA is still evident.

The magnitudes of the residual PM distributions (|residual PM|) for YMS1 and YMS2 are presented in Figures 4(c) and (f), respectively. The rms values are estimated as $0.072 \pm 0.003$ mas yr$^{-1}$ for YMS1 and $0.097 \pm 0.003$ mas yr$^{-1}$ for YMS2, respectively.

### 4.2. YMS3

Figure 5(a) shows the observed bulk PM of YMS3. The spatial distribution of the stars in YMS3 is more spatially spread than in YMS1 and YMS2. This population does not exhibit significant rotation in their bulk PM, as the model variant that includes rotation fails to achieve convergence in the MCMC sampler. We estimate a slightly larger ($\mu_{\rm W,com}$, $\mu_{\rm N,com}$) for YMS3 ($-0.728 \pm 0.016$, $-1.325 \pm 0.018$) when compared to YMS1 and YMS2, notably in the southern direction. Also,

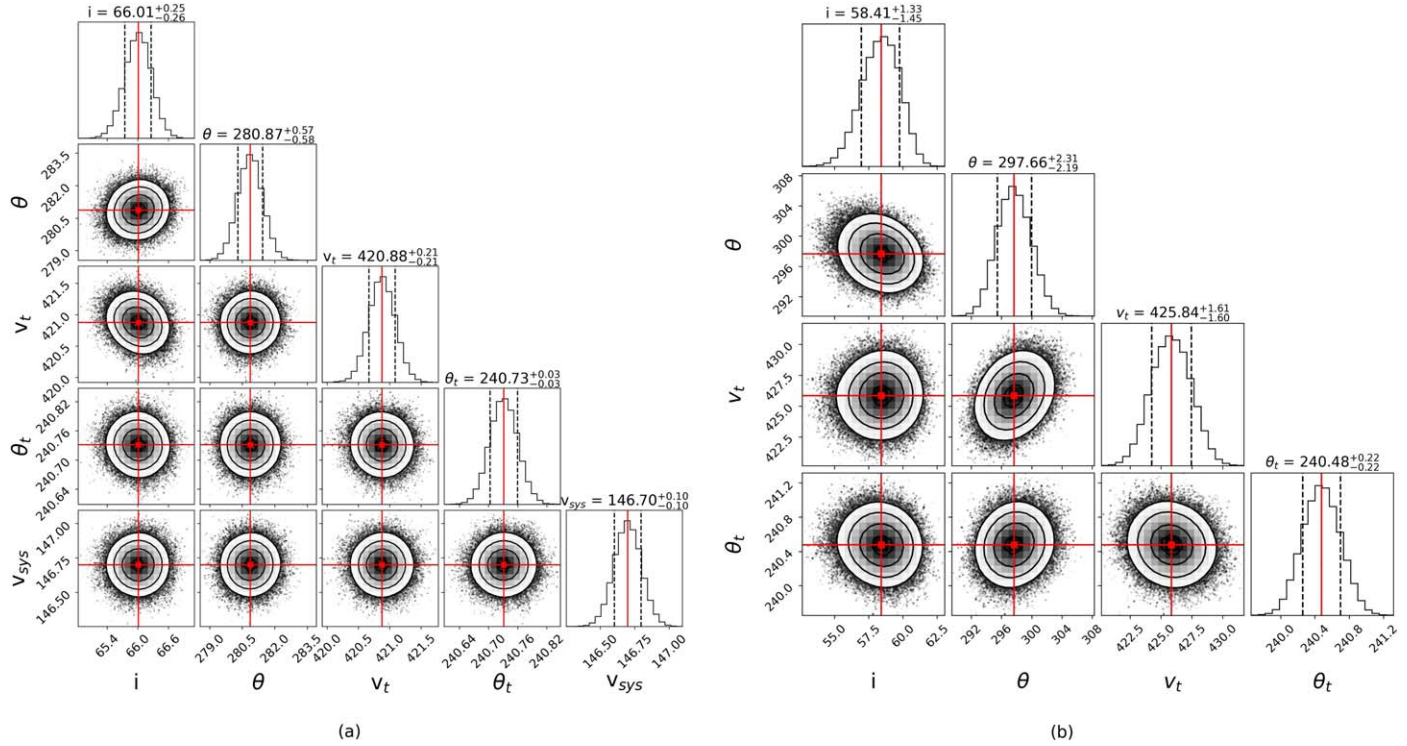


**Figure 3.** The corner plot representing the sampled posterior distribution of kinematic parameters for Red Giants with $v_{\rm los}$ (a) and RGB without $v_{\rm los}$ (b) are shown here. The vertical red lines represent the median values, and the black dashed lines represent the 16th and 84th percentiles.

**Table 1**
The Estimated Kinematic Parameters for the Nine Populations in Our Study are Provided Here

| Data | $i$ (deg) | $\Theta$ (deg) | $v_t$ (km s$^{-1}$) | $\theta_t$ (deg) | $v_f$ (km s$^{-1}$) | $R_f$ (kpc) | $v_{\rm sys}$ (km s$^{-1}$) |
|---|---|---|---|---|---|---|---|
| YMS1 | $81.94^{+0.66}_{-0.67}$ | $185.79^{+3.77}_{-3.61}$ | $420.98^{+2.07}_{-2.08}$ | $242.51^{+0.33}_{-0.32}$ | $88.61^{+11.47}_{-10.38}$ | $8.84^{+1.30}_{-1.21}$ | Fixed |
| YMS2 | $77.68^{+0.90}_{-0.91}$ | $188.92^{+4.19}_{-4.17}$ | $434.21^{+3.04}_{-2.92}$ | $240.97^{+0.40}_{-0.39}$ | $49.32^{+10.91}_{-9.44}$ | $5.85^{+1.65}_{-1.52}$ | Fixed |
| YMS3 | $71.34^{+1.38}_{-1.64}$ | $200.29^{+4.55}_{-4.45}$ | $447.52^{+5.37}_{-5.53}$ | $241.20^{+0.59}_{-0.59}$ | ⋯ | ⋯ | Fixed |
| CLSY | $79.93^{+0.78}_{-0.80}$ | $180.46^{+3.44}_{-3.32}$ | $422.80^{+1.39}_{-1.40}$ | $241.26^{+0.20}_{-0.19}$ | $66.59^{+11.28}_{-10.23}$ | $7.12^{+1.40}_{-1.31}$ | Fixed |
| CLSI | $74.80^{+1.46}_{-1.73}$ | $182.14^{+5.44}_{-5.33}$ | $420.80^{+2.32}_{-2.30}$ | $241.28^{+0.31}_{-0.30}$ | $49.73^{+13.69}_{-12.18}$ | $6.33^{+1.86}_{-1.72}$ | Fixed |
| CLSO | $63.30^{+2.35}_{-2.78}$ | $240.44^{+4.65}_{-5.16}$ | $419.58^{+1.88}_{-1.94}$ | $240.65^{+0.24}_{-0.23}$ | ⋯ | ⋯ | Fixed |
| RGB | $58.41^{+1.33}_{-1.45}$ | $207.66^{+2.31}_{-2.19}$ | $425.84^{+1.61}_{-1.60}$ | $240.48^{+0.22}_{-0.22}$ | ⋯ | ⋯ | Fixed |
| RC | $58.20^{+1.51}_{-1.68}$ | $202.00^{+3.22}_{-3.07}$ | $421.91^{+2.31}_{-2.28}$ | $241.18^{+0.32}_{-0.32}$ | ⋯ | ⋯ | Fixed |
| Red Giants (D14) | $66.01^{+0.25}_{-0.26}$ | $190.87^{+0.57}_{-0.58}$ | $420.88^{+0.21}_{-0.21}$ | $240.73^{+0.03}_{-0.03}$ | ⋯ | ⋯ | $146.70^{+0.10}_{-0.10}$ |

**Note.** The position angle of the line of nodes is measured from the north ($\Theta = \theta - 90°$).

the estimated $i$ ($\sim$71°) for YMS3 is lower, and $\Theta$ ($\sim$200°) is slightly larger when compared to YMS1 and YMS2.

Figure 5(b) shows the spatial residual PM for YMS3. The SEA, SA, and WA are present in YMS3. However, the WA in YMS3 shows the northwest-directed motion of the residuals, unlike the west-directed motion observed in YMS2. Additionally, the SA in YMS3 extends $\sim$6° farther south than in YMS2. Also, the northern and southern outskirts of YMS3 exhibit higher residual PM magnitudes compared to YMS2. As a result, YMS3 shows a broader |residual PM| distribution in Figure 5(c), with an rms value of 0.224 $\pm$ 0.004 mas yr$^{-1}$.

### 4.3. Clusters

The clusters belonging to CLSY and CLSI show rotation signatures. We estimate $v_f$ and $R_f$ to be $\sim$67 km s$^{-1}$ and $\sim$7 kpc, respectively, for CLSY, and $\sim$50 km s$^{-1}$ and $\sim$6 kpc, respectively, for CLSI. This is consistent with the estimated kinematics of YMS1 and YMS2. We also note the absence of significant rotation in the case of older clusters (CLSO with ages >1 Gyr), similar to the kinematics of YMS3. The COM PM also does not show any significant deviation among the cluster groups with respect to the YMS1 and YMS2 populations. However, the estimated $i$ decreases from $\sim$80°

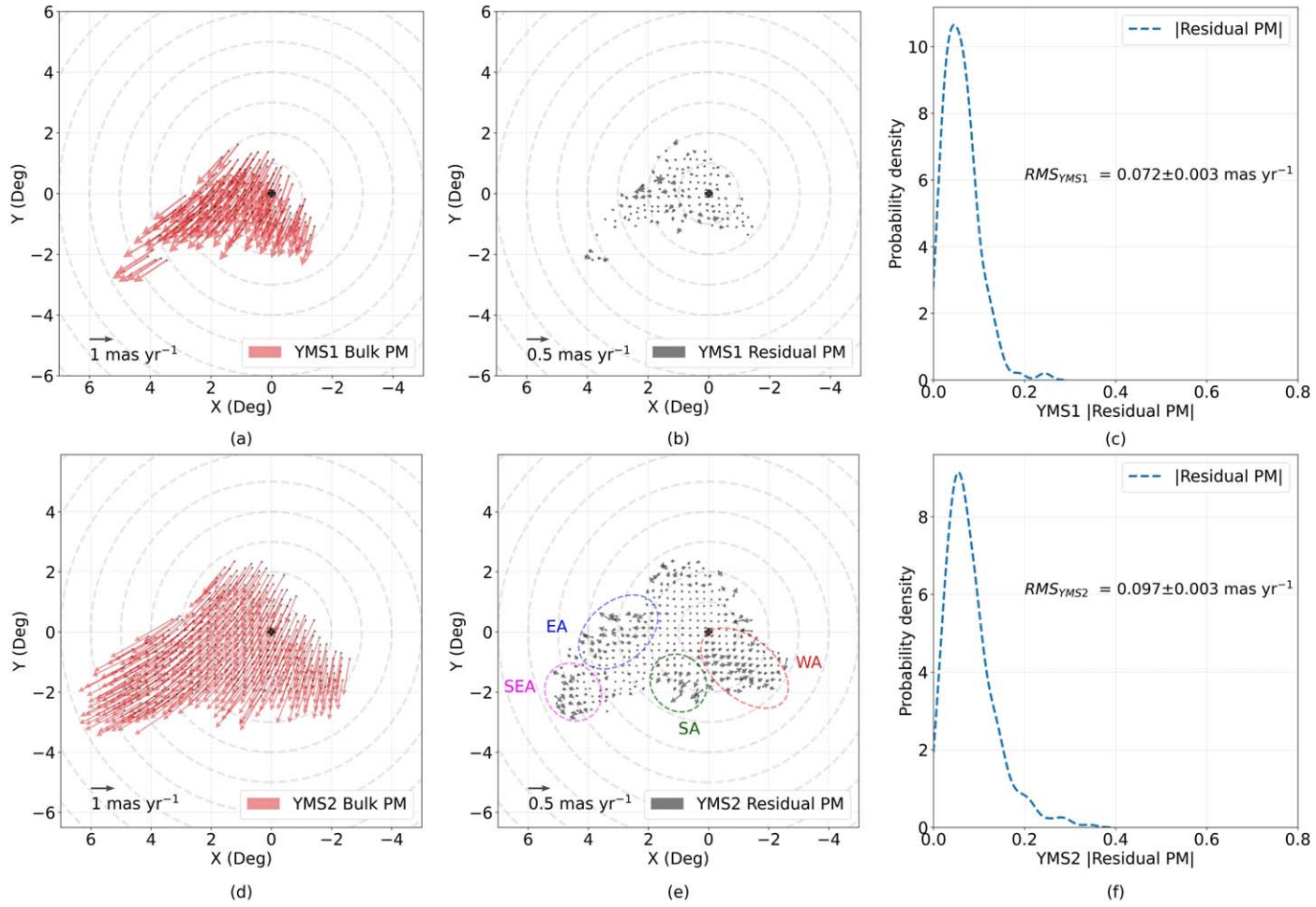


**Figure 4.** The observed PMs ((a) and (d)), residual PM vectors ((b) and (e)), and distributions of |residual PM| ((c) and (f)) for YMS1 and YMS2 are shown here. The EA, SEA, SA, and WA regions identified in the residual PM map of YMS2 are highlighted.

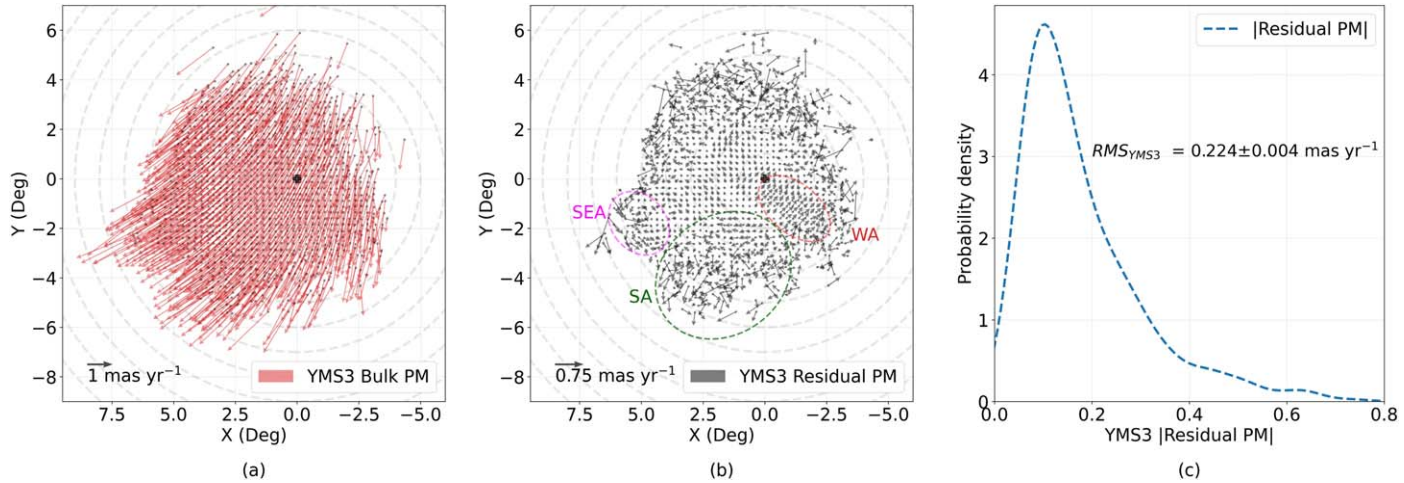


**Figure 5.** The observed PM (a), residual PM vectors (b), and distribution of the |residual PM| (c) for YMS3 are shown here. The SEA, SA, and WA regions identified in the residual PM map of YMS3 are highlighted.

for CLSY (young) to ∼63° for CLSO (old), while Θ increases from ∼180° to ∼240°, similar to the trend seen in the YMS population.

Figure 6(a) shows the observed bulk PM for the clusters belonging to the CLSY group. The clusters in our study are predominantly located in the eastern region of the SMC. Figures 6(b) and (c) show the spatial map and distribution of the magnitude of the residual PM for CLSY. We note the residual PM vectors overall display a relatively more random orientation, along with several clusters showing a larger magnitude of residuals. The distribution of the |residual PM| for CLSY gives an rms value of 0.129 ± 0.007 mas yr$^{-1}$, which is less compared to YMS3, but more than what was found for YMS1 and YMS2. Due to the sparseness, we do not

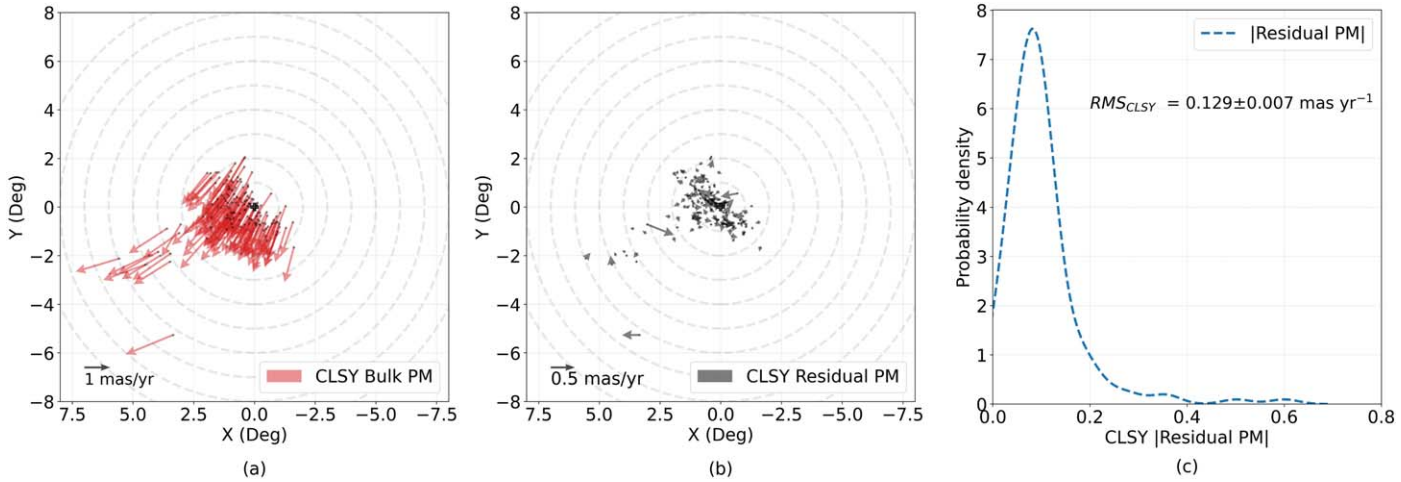


**Figure 6.** The observed PM (a), residual PM vectors (b), and distribution of the |residual PM| (c) for CLSY are shown here.

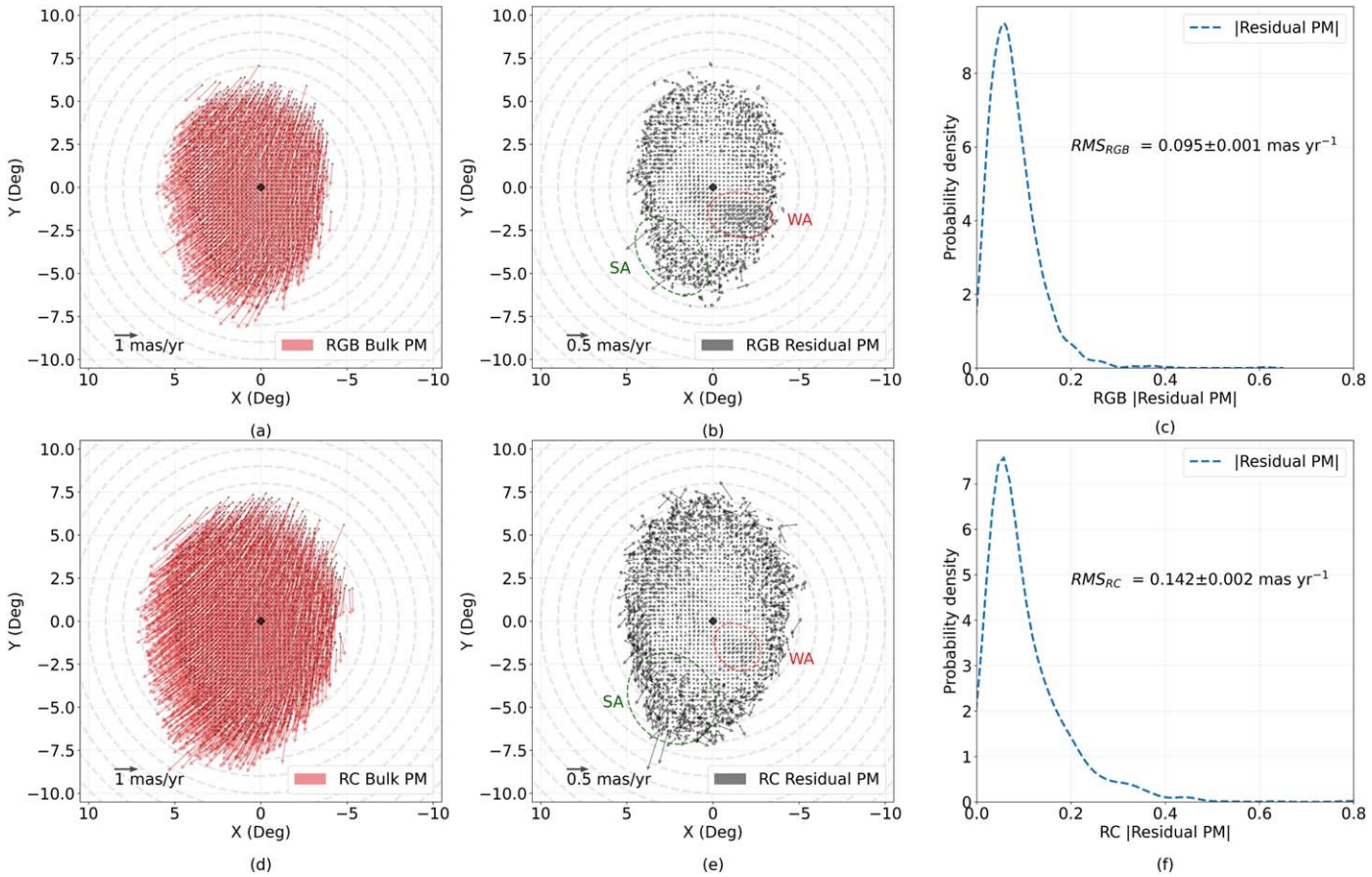


**Figure 7.** The observed PMs ((a) and (d)), residual PM vectors ((b) and (e)), and distributions of the |residual PM| ((c) and (f)) for RGB and RC are shown here. The SA and WA regions identified in the RGB and RC residual PM maps are highlighted.

detect the EA, SEA, SA, or WA in the cluster distribution. Also, we do not show the residual PM maps for CLSI and CLSO, due to their sparse distribution in our sample.

### *4.4. RGB and RC*

Figures 7(a) and (b) present the spatial map of the observed bulk PM for the RGB and RC populations, respectively. The spatial coverages of RGB and RC are similar, although RC extends slightly more toward the outskirts of the SMC. They do not support rotational components in their bulk PMs. The estimated COM PM values for RGB and RC are comparable and do not exhibit significant deviations when compared to other populations, except for YMS3. However, the estimated $i$ is smaller, $\sim$58°, while the $\Theta$ is estimated to be larger than 200°.

Figures 7(b) and (e) depict the spatial maps of the residual PM vectors for RGB and RC, respectively. The EA identified in YMS2 is observed beyond $\sim$3° and is slightly shifted northeast for both RGB and RC. Additionally, the SA extends

beyond ∼4° to the south. However, the WA is more prominently evident for RGB than for RC. In the outskirts of the SMC, the residual PMs are notably pronounced in the RC, especially in the northern and southern regions.

The distributions of the |residual PM| for RGB and RC are shown in Figures 7(c) and (f), respectively. The RC displays a higher rms value of $0.142 \pm 0.002$ mas yr$^{-1}$, compared to $0.095 \pm 0.001$ mas yr$^{-1}$ for RGB.

### 4.5. Red Giants with LOS Velocities

The estimated parameters for Red Giants with radial velocities ($v_{\rm los}$) do not significantly deviate from the model parameters estimated for the RGB and RC populations without $v_{\rm los}$. The $i$ (∼66°) and Θ (∼191°) of the Red Giants are slightly deviant from the 2D model values for the RGB and RC, though these are still notably different from those of the younger MS population. Despite these differences, we do not observe any significant offset in the COM PM for Red Giants relative to the other populations. We estimate a systemic velocity ($v_{\rm sys}$) of $146.70^{+0.10}_{-0.10}$ for the Red Giants, which is closer to the assumed value of 145.6 km s$^{-1}$ used in the 2D modeling of other data sets. Since the radial coverage of Red Giants with $v_{\rm los}$ is smaller (∼3°), and we model individual stars rather than binning them, we do not discuss the residual PM maps.

The various populations in the SMC exhibit distinct kinematic properties, which aid understanding of the kinematic structure of the SMC based on age. In the following section, we discuss the intriguing details that emerge from our modeling.

## 5. Discussion

In this study, we have carried out kinematic modeling of the SMC by analyzing nine different stellar populations, including YMS1, YMS2, YMS3, CLSY, CLSI, CLSO, RGB, RC, and Red Giants.

In the following sections, we discuss the key results from our modeling. We compare the estimated kinematic parameters with those from previous studies, analyze the morphology of the galaxy, examine anomalies in the galaxy's internal motion, and explore the tidal evolution of the SMC.

### 5.1. Kinematic Parameters

The estimated values of ($\mu_{\rm W,com}$, $\mu_{\rm N,com}$) of the SMC from our study are compared with those from previous studies by C11, K13, V16, Z18, G18, D20, and N21 in Table 2 and illustrated in Figure 8. The COM PM values for clusters (CLSY, CLSI, and CLSO), RGB, RC, and Red Giants (with $v_{\rm los}$) do not show significant offsets with respect to the recent estimates (D20 and N21). However, YMS1, YMS2, and YMS3 progressively exhibit offsets in the parameter space, with YMS3 displaying the largest offset.

We note that the YMS3 population has ages between 1 and 2 Gyr, whereas YMS1 and YMS2 are younger than 400 Myr. Also, YMS3 shows a significantly high COM PM directed southward (see Table 2 and Figure 8). The largest southward shift seen in YMS3 could be linked to the encounter between the LMC and the SMC about 1.5 Gyr ago (D24). This may be a sign that these stars probably retain the kinematic disturbance of the gas from which they are born, as a result of the interaction. CLSO (ages >1 Gyr) does not show this trend, since the clusters are smaller in number in this group.

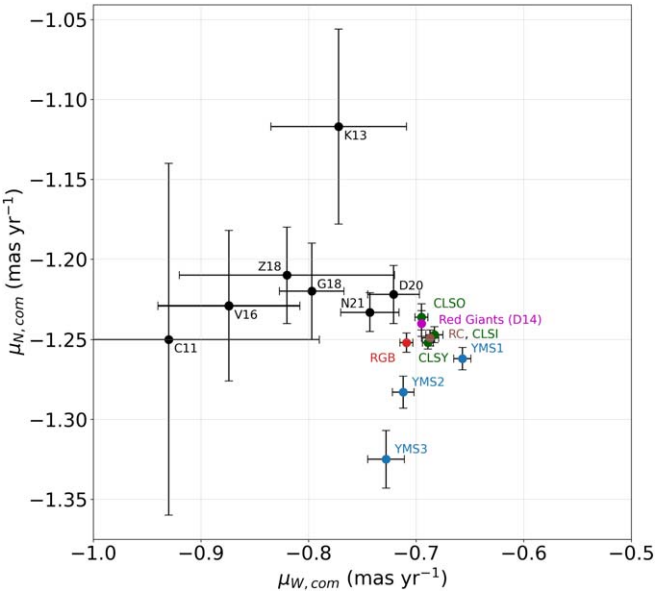


**Figure 8.** The parameter space of the estimated ($\mu_{\rm W,com}$, $\mu_{\rm N,com}$) is compared with the reference studies (provided in Table 2). The corresponding estimated parameters for YMS1, YMS2, and YMS3 are marked with blue dots. The clusters are marked with green dots. RGB, RC, and Red Giants are marked with red, brown, and magenta dots, respectively. The reference studies are marked with black dots. Error bars are provided as well.

**Table 2**
Comparison of the Estimated COM PMs with Previous Studies

| $\mu_{\rm W,com}$ (mas yr$^{-1}$) | $\mu_{\rm N,com}$ (mas yr$^{-1}$) | References |
|---|---|---|
| $-0.657 \pm 0.008$ | $-1.262 \pm 0.007$ | YMS1 |
| $-0.712 \pm 0.010$ | $-1.283 \pm 0.010$ | YMS2 |
| $-0.728 \pm 0.017$ | $-1.325 \pm 0.018$ | YMS3 |
| $-0.704 \pm 0.004$ | $-1.252 \pm 0.005$ | CLSY |
| $-0.687 \pm 0.005$ | $-1.247 \pm 0.008$ | CLSI |
| $-0.683 \pm 0.008$ | $-1.236 \pm 0.006$ | CLSO |
| $-0.695 \pm 0.006$ | $-1.252 \pm 0.005$ | RGB |
| $-0.687 \pm 0.008$ | $-1.249 \pm 0.008$ | RC |
| $-0.687 \pm 0.008$ | $-1.249 \pm 0.008$ | Red Giants |
| $-0.743 \pm 0.027$ | $-1.233 \pm 0.012$ | N21 |
| $-0.721 \pm 0.024$ | $-1.222 \pm 0.018$ | D20 |
| $-0.82 \pm 0.10$ | $-1.21 \pm 0.03$ | Z18 |
| $-0.797 \pm 0.030$ | $-1.220 \pm 0.030$ | G18 |
| $-0.874 \pm 0.066$ | $-1.229 \pm 0.047$ | V16 |
| $-0.772 \pm 0.063$ | $-1.117 \pm 0.061$ | K13 |
| $-0.93 \pm 0.14$ | $-1.25 \pm 0.11$ | C11 |

**Note.** The first nine rows list the estimations from this study.

The estimated value of $i$ for most of the old to young population in our study ranges from ∼58° to 82°, while Θ ranges from ∼185° to 202°. This range aligns with the findings of Z21 using Gaia DR2 data, which reported a value of $i$ between 50° and 80° and Θ of ∼180°. S15 estimated ($i$, Θ) of ∼(64°, 155°) using Cepheids. Meanwhile, D18 estimated these values to be ∼(51°, 66°) using H I gas. The sparse distribution of CLSO, along with the central concentration of clusters in our sample, results in a larger Θ value (∼240°). However, our estimations tentatively suggest a decreasing value of $i$ and an increasing value of Θ with the increase in age of the tracer population.

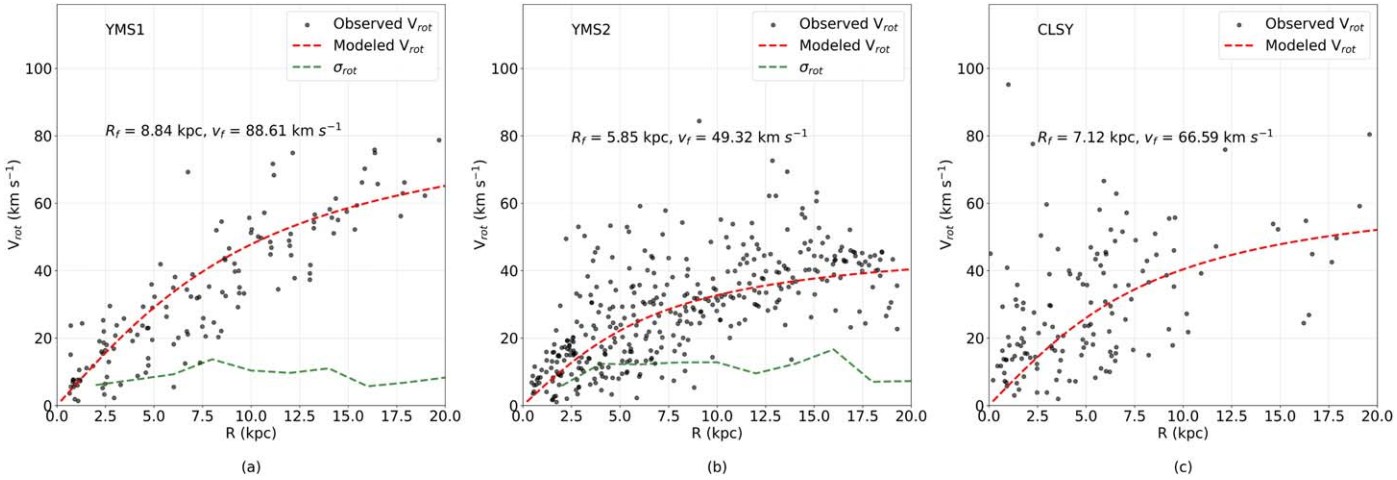


**Figure 9.** The rotation velocity ($V_{\rm rot}$) profile of the SMC is shown for YMS1 (a), YMS2 (b), and CLSY (c) in the SMC plane. The black dots represent the observed $V_{\rm rot}$, while the red dashed curve denotes the modeled $V_{\rm rot}$. The dispersion ($\sigma_{\rm rot}$) of the observed $V_{\rm rot}$ for the YMS1 and YMS2 populations is shown with the green dashed curve.

The bin sizes for binning the Gaia data are set at $0.^{\circ}25$, to visually identify the features seen in the PM and residual PM maps (Section 2). Modifying the bin sizes, either by increasing or decreasing them, as well as altering the minimum requirement of five stars per bin for estimating the median PM, does not substantially affect the parameter estimates in this study. We modified the bin sizes and the minimum number of stars per bin, but found that the parameter estimates did not change significantly across all the populations. Therefore, the estimated COM PMs and viewing angles ($i$ and $\Theta$) for the SMC in our study are reliable and consistent with the findings of previous studies.

### 5.2. Internal Rotation of the SMC

The younger populations show evidence of internal rotation in the SMC. The values of $v_f$ we estimated in this study are ∼89 and 49 km s$^{-1}$ for YMS1 and YMS2, respectively. However, in our study, we estimated a larger $R_f$ of ∼9 and 6 kpc for YMS1 and YMS2, respectively, compared to the estimates by D18 ($R_f \sim 1.1$ kpc). A comparable trend is observed in the cases of CLSY and CLSI. We were not able to fit the rotation component for YMS3, CLSO, RGB, and RC, but we noted a partial convergence of $v_f$ below 8 km s$^{-1}$, which is not reliable, as the error in the estimations is of the order of 10 km s$^{-1}$ (noted in YMS1 and YMS2). This suggests that the rotation in the old population is significantly less and can be assumed to have no rotation. This is consistent with the study by Z21, which found a moderate or slow rotation of ∼10 km s$^{-1}$ in the central regions of the SMC using Red Giant stars.

Figures 9(a) and (b) show the rotation velocity profiles for YMS1, YMS2, and CLSY, respectively. The rotation velocity within the SMC plane ($V_{\rm rot}$) is presented as a function of the galactocentric distance ($R$, in kiloparsecs). We also estimated an average rotational dispersion ($\sigma_{\rm rot}$) of ∼9 and 11 km s$^{-1}$ for YMS1 and YMS2, respectively. This was done using a binning interval of 2 kpc along the disk radius. In CLSY, the absence of enough clusters beyond the radius of 11 kpc prevents the estimation of $\sigma_{\rm rot}$. The smaller values of $\sigma_{\rm rot}$ suggest a disk morphology for the younger population (YMS1 and YMS2). The extension of $R$ to ∼20 kpc or more indicates that the disk structure of the SMC is notably more stretched along the galaxy plane for the younger populations compared to its appearance in the sky plane.

For the cluster groups CLSY and CLSI, we found evidence of rotation consistent with the YMS1 and YMS2 populations. However, the cluster samples in the wing region of the SMC are sparse in our study, leading to variations in $i$ and $\Theta$ between the young clusters (CLSY and CLSI) and the young MS populations (YMS1 and YMS2).

In the next section, we present the in-plane morphology of the SMC based on our model.

### 5.3. Morphology of the SMC

Figure 10 shows the 3D perspective of the SMC for different populations (YMS1, YMS2, YMS3, RGB, and RC) based on the disk models we obtained in our study. The distances in $X$–$Y$–$Z$ (in kiloparsecs) are estimated based on the fixed center ($\alpha_0 = 13.^{\circ}05$; $\delta_0 = -7.^{\circ}83$) and the mean distance ($D_0 = 62.44$ kpc) to the galaxy center. Figure 10(a) shows the density distributions of different populations as observed in the sky plane, where the negative $X$- and $Y$-directions are the east and south directions, respectively. Figure 10(b) shows the $X$–$Y$–$Z$ perspective of the SMC, which is attained by a clockwise rotation of 90° about the $X$-axis ($Y = 0$), $R_1 = 90°$, and followed by another clockwise rotation of 20° about the new $Y$-axis, $R_2 = 90°$. This keeps much of the population on the edge-on perspective, which also reflects their varying values of $i$ for the disk. The RC and RGB disk has an offset of more than 19° with YMS1 and YMS2. Figure 10(c) shows an alternative $X$–$Y$–$Z$ perspective of the SMC for $R_1 = 90°$ and $R_2 = 120°$, obtained after performing the rotations from the sky-plane perspective of Figure 10(a). The selection of $R_1$ and $R_2$ is arbitrary and only serves to visualize the disk's inclination and the spatial distribution of different populations on the galaxy plane.

The triangular density distribution of the young population (YMS1 and YMS2) in the sky plane appears similar to that of the observed density distribution of H I in the SMC (N. Loiseau & Bajaja 1981, S04). The distribution of the older population (RGB and RC) in our study appears elliptical in the sky plane (Figure 10(a)). Also, the previous studies suggest that the old population of the SMC is distributed in a spheroidal or ellipsoidal shape (J. Harris & D. Zaritsky 2004; R18; Y19). Our

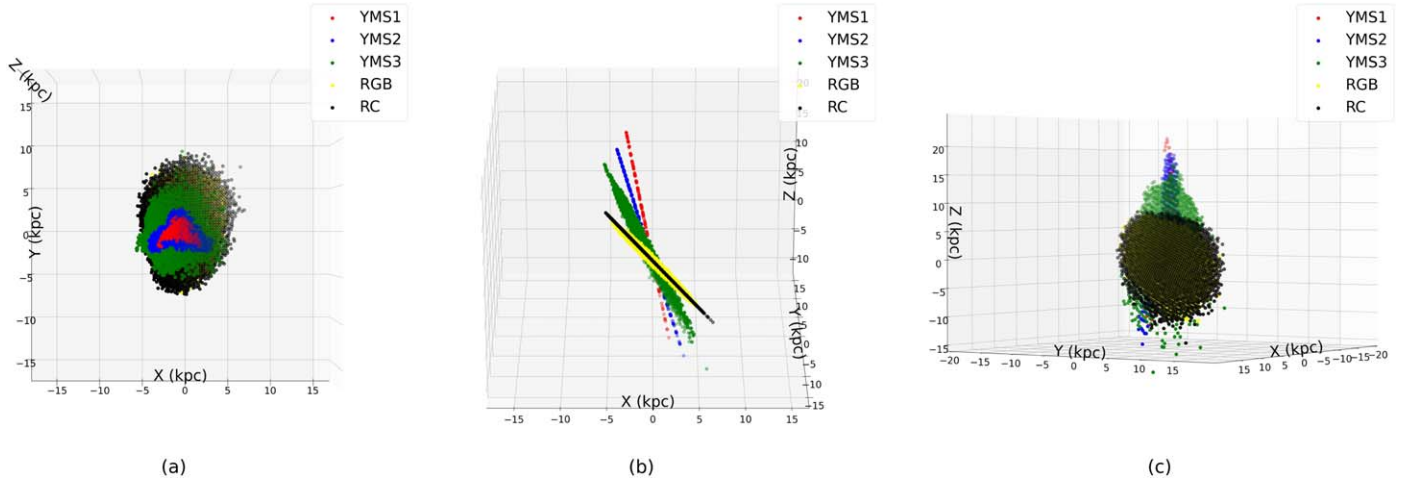


**Figure 10.** The distribution of the YMS1, YMS2, YMS3, RGB, and RC populations in our study are color-coded and depicted. (a) Populations in the sky-plane perspective ($X$–$Y$ plane). (b) $X$–$Y$–$Z$ perspective 1: $(R_1, R_2) = (90°, 20°)$. (c) $X$–$Y$–$Z$ perspective 2: $(R_1, R_2) = (90°, 120°)$. $R_1$ represents a clockwise rotation about the $X$-axis of the sky-plane perspective, followed by $R_2$, which is a subsequent clockwise rotation about the new $Y$-axis.

model indicates a highly inclined morphology for the SMC across all populations. We find that YMS1 and YMS2 are rotation-supported, while for the old population, we likely traced a projected geometry of an ellipsoidal distribution along the semimajor and semiminor axes. Notably, D14 estimated an LOS dispersion of $\sim$26 km s$^{-1}$ for the Red Giants we used in our study. This implies that the SMC probably has a flattened ellipsoidal distribution, where the younger populations (YMS1 and YMS2) have rotation-supported disk structures.

Figures 10(b) and (c) reveal the LOS depth of the SMC based on the disk morphology obtained in this study for both young and old populations. Figure 11 shows the estimated LOS distance ($D$, in kiloparsecs) of the clusters (CLSY, CLSI, and CLSO) in our study plotted against their age (in gigayears). The data are color-coded according to the extinction in the Gaia G band ($A_G$). The age and extinction values are taken from D24. We compare this plot with a similar plot by A. E. Piatti (2022—hereafter, P22) using clusters in the outer northeast of the SMC. We note a trail of young clusters (<200 Myr) in Figure 11 along the decreasing LOS distance (east of the SMC), which was noted in P22 as well. These clusters are also oriented along the wing region of the SMC, suggesting they were formed after the recent SMC–LMC interaction. The estimation of cluster ages in our previous study (D24) did not take disk morphology into account. Hence we re-estimated the ages of the clusters using the current LOS distances obtained using the disk model of the clusters. However, we observed minor differences in the estimates that fall within the margins of the error for age estimation. The LOS depth for clusters, determined from the estimated inclination relative to the center, is $\sim$20 kpc to the east and $\sim$12 kpc to the west.

Our model suggests that the LOS depth for the RC and RGB populations extends $\sim$11 kpc to both the east and west of the SMC. In contrast, the LOS extension of the young populations (YMS1, YMS2, and YMS3) in the west surpasses 15 kpc, with the eastern side of YMS1 extending to $\sim$20 kpc. The studies by J16 and R17 previously reported the younger population of the SMC as having an LOS elongation of $\sim$20 kpc. In essence, our models trace both the younger and older populations having a larger LOS depth, consistent with previous observations.

To better visualize the disk plane of the SMC, we present RC, RGB, YMS3, YMS2, CLSY, and YMS1 within their best-fitting

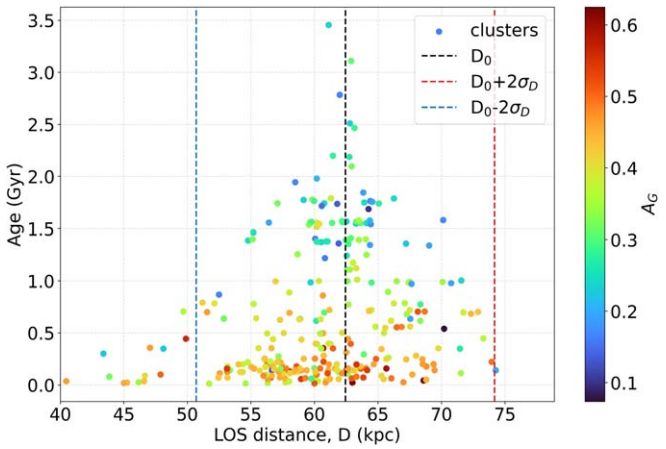


**Figure 11.** The age distribution of the clusters (CLSY, CLI, and CLSO) is shown here according to their LOS distance (D), with each cluster color-coded based on extinction in the Gaia $G$ band ($A_G$). $D_0 =$ 62.44 kpc is the adopted mean distance to the SMC, with $\sigma_D$ representing the standard deviation in D based on the disk model.

disk plane of the galaxy ($X'$–$Y'$-axes), as shown in Figure 12. Each population's disk plane is rotated counterclockwise by their corresponding $i$ and about the position angle of the line of nodes axis. Also, each source is color-coded based on the LOS distance ($D$, in kiloparsecs) as well. This perspective aligns the disk plane with the standard east, west, north, and south directions of the sky plane, facilitating a comparison of the disk plane and its appearance in the sky. Starting with the RC and RGB populations, we observe that the SMC extends up to $\sim$10 kpc from its center. The YMS3 population, which is 1–2 Gyr old, is more spread out, but elongated compared to the RC and RGB, reaching over $\sim$17 kpc from the SMC center. In contrast, YMS1, YMS2, and CLSY, which are less than 400 Myr old, exhibit an even larger stretch in their disk distributions. These populations are significantly more elongated along the $X'$-axis compared to the Y′-axis, extending up to $\sim$20 kpc from the center, with YMS1 and CLSY spanning more than 22 kpc. However, we estimated a small dispersion of $\sim$10 km s$^{-1}$ in the rotation profiles for YMS1 and YMS2 (Figures 9(a) and (b)). This suggests that the young SMC likely has a disk structure that is

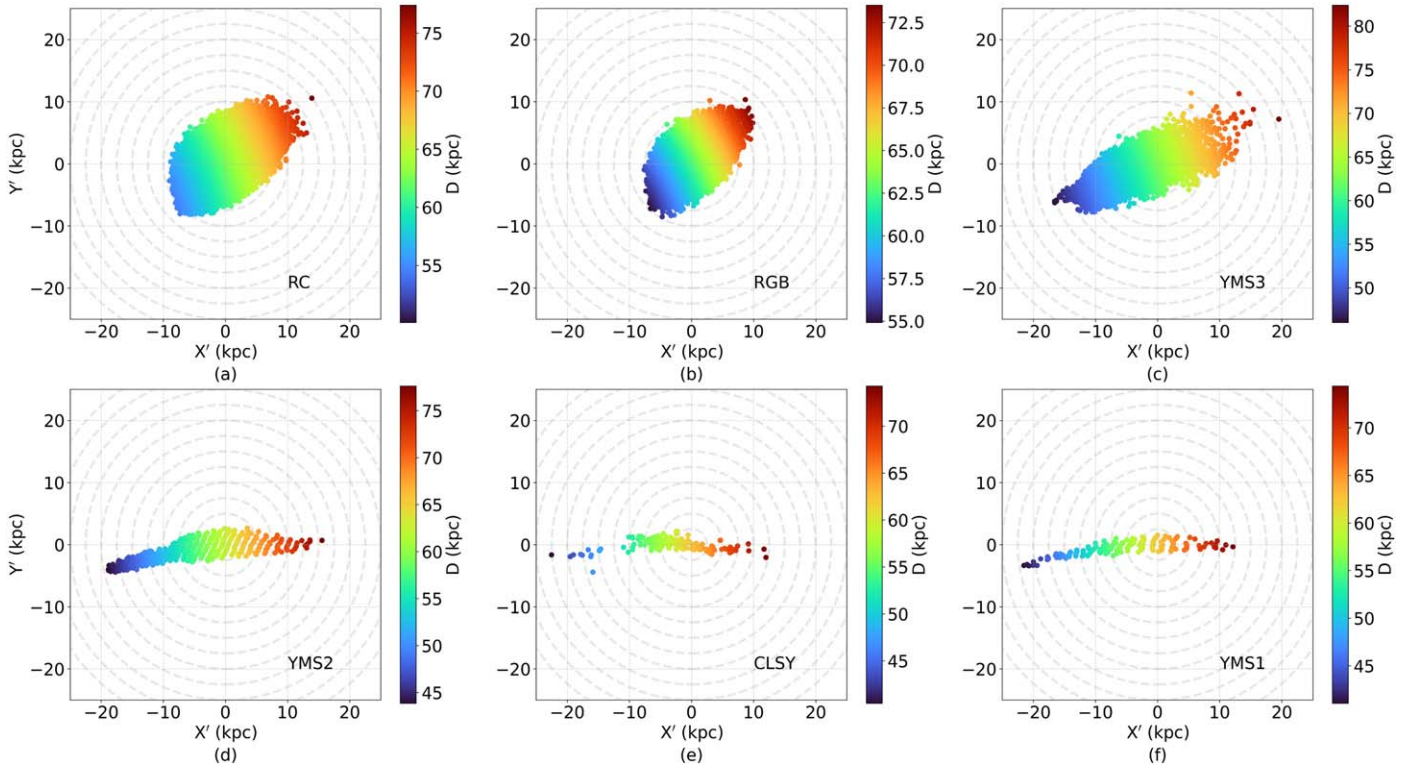


**Figure 12.** The morphology of the SMC is shown in the disk plane (primed coordinates) of the galaxy. (a)–(f) RC, RGB, YMS3, YMS2, CLSY, and YMS1, respectively. The sources in each population are color-coded with the LOS distance ($D$, in kiloparsecs) as well.

not very thick. Additionally, the appearance of RC and RGB indicates a more compact ellipsoidal structure compared to the young populations.

In the following section, we will investigate the anomalies identified in the residual PM maps in conjunction with the SMC's morphology.

### *5.4. Anomalies in the Kinematics and Tidal Evolution of the SMC*

The anomalies we identified in the residual PM map of YMS2 (Section 4) are evident in both the young and the old populations. The SEA, which represents a stellar population in counter-rotation, is noticed for the first time in the SMC, and it is prominent across YMS1, YMS2, and YMS3. The appearance of counter-rotation in the residual could arise due to the slower rotation of the population with respect to the model (this is explored further in detail later). The EA indicates the motion of groups of stars away from the SMC and directed toward the LMC along the young bridge of the SMC. We note the clusters in the east wing are mostly of ages less than 200 Myr; they also have residual PMs aligned toward the younger bridge. However, the SA shows the residual PM vectors of the stellar population aligning to the south on the SMC outskirts, probably connecting to the old bridge.

The eastward movement of stars in the younger population toward the younger bridge was previously noted in the study by N21 and aligns with our findings. Figure 16 of G21 illustrates comparable movements of both old and young populations toward the older and younger bridges, respectively, which is consistent with our findings. The residual PM features located beyond $\sim 5^\circ$ to $\sim 8^\circ$ for RGB and RC (as shown in Figures 7(b) and (e)) show similarities to the trends observed by L. R. Cullinane et al. (2023) for the offset population of RGB stars on the SMC outskirts, as depicted in their Figure 4.

The WA is observed in the central regions and extends mostly westward in the SMC, which is evident in both young and old populations (YMS2, YMS3, RGB, and RC). The west-directed motion of these populations is consistent with the studies by F. Niederhofer et al. (2018) and B. Dias et al. (2022). The motion is directed to the west halo of the SMC, a tidal feature suggested by B. Dias et al. (2016). The west halo is later associated with the counter-bridge of the SMC (B. L. Tatton et al. 2021), which loops behind the SMC from the southwest to the northeast of the galaxy.

The anomalies observed point out that the galaxy is showing tangential anisotropy in PM across all the populations. We further analyze the observed internal $PM_X$ and $PM_Y$ along the $X$-direction for YMS2 and YMS1, aiming to assess their respective contributions to these four anomalies. Figures 13(a) and (c) illustrate the variation in the $X$-component of the internal PM ($PM_X$) for YMS2 and YMS1 along the $X$-direction in the sky plane. Meanwhile, Figures 13(b) and (d) depict the variation in the $Y$-component of the internal PM ($PM_Y$) for YMS2 and YMS1 along the same $X$-direction in the sky plane. The color-coding for the anomalies in both YMS1 and YMS2 across each panel is based on the EA, SEA, SA, and WA regions identified in YMS2. This facilitates a region-to-region comparison between YMS2 and YMS1.

The SEA is found to have larger values of ($PM_X$), indicative of an inward motion, and lower values for ($PM_Y$), indicative of slower rotation, particularly for regions at $X \sim 4^\circ$ and beyond, as seen in Figures 13(a) and (b). Furthermore, the SEA region in YMS1, as shown in Figures 13(c) and (d), noticeably has a reduced number of bins compared to YMS2. This suggests that the disk's rotation is attaining stability in the youngest

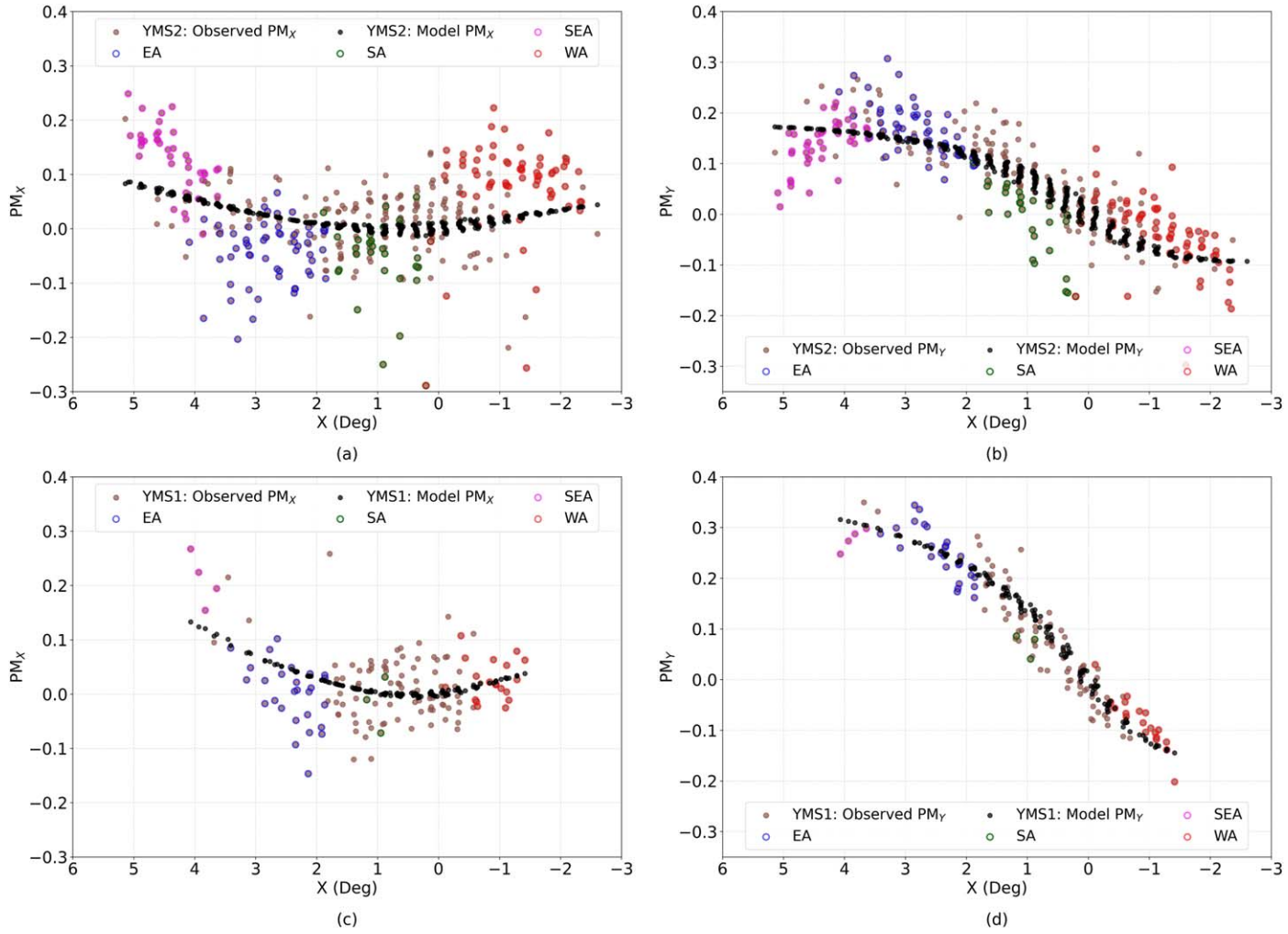


**Figure 13.** Comparisons of the internal PM components ($PM_X$, $PM_Y$) along the $X$-direction of the sky plane for YMS2 and YMS1 are shown here. The observed $PM_X$ and $PM_Y$ are represented by brown dots, while their corresponding model predictions are indicated by the black dots. The SEA-, EA-, SA-, and WA-binned stars identified for YMS2 (see Section 4.1) are marked with the magenta, blue, green, and red circles, respectively.

population (YMS1). The SEA prominently emerges from the YMS3 population (ages ∼1 to 2 Gyr) and is not so evident in RGB and RC. This suggests that the SEA is predominantly detected in the populations with a ∼50 Myr to 2 Gyr age range. Our models indicate that the SMC's rotation starts with the YMS2 population, suggesting that the SEA may be pointing to a gas infall from the outskirts into the southeastern region of the SMC, where stars formed from this gas retaining the infalling gas kinematics. We therefore classify the SEA to be an infalling feature, rather than a counter-rotating feature.

The EA reveals larger negative values in $PM_X$, and it is evident in both YMS2 and YMS1. The inner bins in the east between ∼2° and 4° of YMS2 show large negative observed $PM_X$ values, suggesting an eastward-directed motion. This implies that stars in these bins are being pulled eastward toward the LMC. In the YMS1 population, the bins of stars in the central regions between 1° and 3° exhibit a similar eastward motion, along with larger negative values for $PM_X$. This points to the tidal signature in the RA direction likely resulting from the SMC interacting with the LMC.

The SA reveals the flow of stars toward the south of the SMC, which is prominent in the YMS2 population and only marginally present in YMS1. The outward motion of binned stars to the south is also observed in the YMS3, RGB, and RC populations, suggesting that this is likely associated with the old bridge of the SMC.

The WA appears prominently in YMS2 but not in YMS1. The more positive values of $PM_X$ observed for WA when compared to the model are suggestive of a westward motion. There is a marginally higher value for these populations in the $PM_Y$ when compared to the model, suggesting a northward motion. The predominantly westward motion of stars present in YMS2 is missing in YMS1. If the gas in these regions is also affected by this motion, then the gas can escape the SMC through the western halo. This could explain the contribution of gas to the Magellanic Stream, which in turn could explain the absence of stars in YMS1 for values of $X < -1°$ (Figure 12(c)). Notably, all the anomalies (SEA, EA, SA, and WA) show greater anisotropy in $PM_X$ than in $PM_Y$, which is a result of the line of interaction with the LMC. Additionally, the variation of $PM_X$ and $PM_Y$ along the $Y$-direction shows similar anomalies.

The morphology of the young SMC, as seen in the SMC plane, appears to be extensively stretched in the east–west direction. This stretching is starting to appear in the YMS3 population and is full-blown in the distribution of the YMS2 population. The contrasting distribution of the RC/RGB (Figures 12(a)/(b)) to YMS2 (Figure 12(d)) highlights the skewed stellar distribution. The morphological change is

suggestive of a stretched distribution of the gas that is formed in the younger populations. We explore the possible connection of this feature with the tidal effects of the LMC–SMC interaction. The eastward motion is likely to be associated with the recent interactions between the LMC and the SMC, as evidenced by the eastward stretch across all populations. Similarly, the westward motion is evident across all populations, but less pronounced in YMS1. These two interaction signatures, which are acting along the same line, but in opposite directions of the SMC's internal PM, suggest that its elongation is a result of the significant tidal stretching, particularly from the recent interaction, as it is most pronounced in YMS2. Moreover, the increased inclination of the younger population has resulted in smaller LOS distances in the eastern part, along with a significant reduction in the extent of the SMC in the north–south direction. All these point to a significant tidal influence from its larger companion. The fact that all anomalies exhibit more deviation in the $X$-direction of the PM is also suggestive of extensive tidal signatures across the SMC. The tangential anisotropy on the PM of the SMC has previously been observed in the RA direction of the galaxy, which is associated with the tidal disruption of the dwarf galaxy due to the gravitational influence of the LMC (J. Klimentowski et al. 2007; D18; S. Hota et al. 2024). Similarly, several studies have reported tidal stripping or stretching of the SMC (A. E. Piatti 2021, N21, D. El Youssoufi et al. 2023), which aligns with the picture of the SMC emerging from our models. The counter-rotating signature that is identified in this study for the first time is unlikely to be a tidal signature but rather a hydrodynamic one, probably from the gas infall during the course of the morphological evolution of the SMC.

This study provides baseline models estimated from the median motion as traced by the majority of the stellar populations across the SMC. The anomalies detected in the residual PMs of the different stellar populations are likely to be the major outliers as they are shown by the bulk of the population. This study therefore does not detect kinematic and structural outliers that exist in smaller fractions of the population across the SMC. Therefore, we note that the base models derived here will be very helpful in detecting the kinematic and structural outlier (minority) populations that exist in the SMC. The unique PM pattern identified in this study can aid numerical simulations in pinpointing the details of the interaction between the MCs. However, the anomalies seen in the residual PM maps of this study need further investigation, such as a 3D model including the radial velocity for all populations, to fully comprehend the dynamic evolution of the SMC.

## 6. Summary

We summarize the results and conclusions derived from the disk model of the SMC using Gaia DR3 data.

1. We have performed kinematic modeling of the SMC using nine different populations to investigate the galaxy's morphology. Eight populations were used to derive a 2D model, using PMs from Gaia DR3, and one was used to derive a 3D model using the PM (Gaia DR3) and radial velocities. The data coverage of the SMC considered in this study is within $\sim 7.^{\circ}5$ of the galaxy center.
2. The best-fitting kinematic parameters of the SMC were estimated using an MCMC method. The parameters estimated in this study—such as the inclination of the SMC disk ($i$), the position angle of the line of nodes measured from the west ($\theta$), the amplitude of the tangential velocity of the SMC's COM ($v_t$), the tangential angle made by $v_t$ ($\theta_t$), the scale radius ($R_f$), the asymptotic velocity ($v_f$), and the systemic velocity ($v_{\rm sys}$)—show good agreement with estimations in the literature when comparisons are made between similar populations.
3. The COM PM for the entire population exhibits minimal variation, except in YMS3, where the southward motion is larger than in other populations. This may be a signature of the LMC–SMC interaction ∼1–2 Gyr ago.
4. We estimate $i$ to range from $\sim 58^{\circ}$ to $82^{\circ}$ and $\Theta$ to range from $\sim 180^{\circ}$ to $240^{\circ}$ among the young and old populations of the SMC. We observe that $i$ decreases with age, while $\Theta$ increases.
5. We estimate $v_f$ of $\sim 89\,{\rm km\,s^{-1}}$ for YMS1 and $49\,{\rm km\,s^{-1}}$ for YMS2, with corresponding $R_f$ of ∼9 and 6 kpc. A similar trend is observed for CLSY and CLSI. This suggests that both YMS1 and YMS2 show a rotation-supported disk structure for ages less than 400 Myr. In contrast, the older populations (YMS3, RGB, RC, CLSO, and Red Giants) do not exhibit significant rotation and are likely pressure-supported.
6. The young MS population (YMS1 and YMS2) shows an elongated structure in the galaxy plane, with a rotational velocity dispersion of $\sim 11\,{\rm km\,s^{-1}}$, suggesting a flattened rotating structure for the SMC.
7. Our models reveal a larger LOS extension for the SMC, reaching up to ∼30 kpc across the different stellar populations (old and young).
8. We identify several anomalies on the residual PM of YMS2, which are the EA, SEA, SA, and WA. The SEA, identified for the first time, is suggestive of an infalling population, possibly having a hydrodynamic origin. The SA is likely associated with the old bridge, while the EA and WA appear to be of tidal origin.
9. This study also brings out the morphological change in the SMC over its evolution. The extensive east–west stretch seen in the young population is likely to be due to the skewed distribution of gas in the SMC resulting from the recent interactions.
10. This preferential stretching in the $X$-direction is also noted in the young stars. The internal rotation of the young population along the $X$-direction ($\rm PM_X$) of the SMC exhibits greater tangential anisotropy than in the $Y$-direction, suggesting that the galaxy is being tidally stretched due to the influence of the LMC.

## Acknowledgments

We thank the referee for valuable suggestions that helped to improve the manuscript. A.S. acknowledges support from the Science and Engineering Research Board (SERB) Power fellowship. This work has made use of optical data from the European Space Agency (ESA) mission Gaia (https://www.cosmos.esa.int/gaia), which was processed by the Gaia Data Processing and Analysis Consortium (DPAC; https://www.cosmos.esa.int/web/gaia/dpac/consortium). The funding for DPAC has been provided by national institutions, particularly

the institutions participating in the Gaia Multilateral Agreement.

*Software:* ASTROPY (Astropy Collaboration et al. 2013, 2018, 2022), SCIPY (P. Virtanen et al. 2020), MATPLOTLIB (J. D. Hunter 2007), NUMPY (C. R. Harris et al. 2020), CORNER (D. Foreman-Mackey 2016).

## ORCID iDs

S. R. Dhanush https://orcid.org/0009-0007-0388-3143
A. Subramaniam https://orcid.org/0000-0003-4612-620X
S. Subramanian https://orcid.org/0000-0002-5331-6098

## References

Astropy Collaboration, Price-Whelan, A. M., Lim, P. L., et al. 2022, ApJ, 935, 167
Astropy Collaboration, Price-Whelan, A. M., Sipőcz, B. M., et al. 2018, AJ, 156, 123
Astropy Collaboration, Robitaille, T. P., Tollerud, E. J., et al. 2013, A&A, 558, A33
Cioni, M. R. L., Habing, H. J., & Israel, F. P. 2000, A&A, 358, L9
Costa, E., Mndez, R. A., Pedreros, M. H., et al. 2011, AJ, 141, 136
Cullinane, L. R., Mackey, A. D., Da Costa, G. S., Koposov, S. E., & Erkal, D. 2023, MNRAS, 518, L25
Deb, S., Kurbah, K., Singh, H. P., et al. 2019, MNRAS, 489, 3725
Deb, S., Singh, H. P., Kumar, S., & Kanbur, S. M. 2015, MNRAS, 449, 2768
DeLeo, M., Carrera, R., Nol, N. E. D., et al. 2020, MNRAS, 495, 98
de Vaucouleurs, G., & Freeman, K. 1972, VA, 14, 163
Dhanush, S. R., Subramaniam, A., Nayak, P. K., & Subramanian, S. 2024a, MNRAS, 528, 2274
Dhanush, S. R., Subramaniam, A., & Subramanian, S. 2024b, ApJ, 968, 103
Dias, B., Kerber, L., Barbuy, B., Bica, E., & Ortolani, S. 2016, A&A, 591, A11
Dias, B., Parisi, M. C., Angelo, M., et al. 2022, MNRAS, 512, 4334
Diaz, J. D., & Bekki, K. 2012, ApJ, 750, 36
DiTeodoro, E. M., McClure-Griffiths, N. M., Jameson, K. E., et al. 2018, MNRAS, 483, 392
Dobbie, P. D., Cole, A. A., Subramaniam, A., & Keller, S. 2014, MNRAS, 442, 1663
D'Onghia, E., & Fox, A. J. 2016, ARA&A, 54, 363
El Youssoufi, D., Cioni, M.-R. L., Bell, C. P. M., et al. 2019, MNRAS, 490, 1076
El Youssoufi, D., Cioni, M.-R. L., Kacharov, N., et al. 2023, MNRAS, 523, 347
El Youssoufi, D., Cioni, M.-R. L., Bell, C. P. M., et al. 2021, MNRAS, 505, 2020
Foreman-Mackey, D. 2016, JOSS, 1, 24
Gaia Collaboration, Helmi, A., van Leeuwen, F., et al. 2018, A&A, 616, A12
Gaia Collaboration, Luri, X., Chemin, L., et al. 2021, A&A, 649, A7
Gardiner, L. T., Sawa, T., & Fujimoto, M. 1994, MNRAS, 266, 567
Goodman, J., & Weare, J. 2010, CAMCS, 5, 65
Graczyk, D., Pietrzyński, G., Thompson, I. B., et al. 2020, ApJ, 904, 13
Hammer, F., Yang, Y. B., Flores, H., Puech, M., & Fouquet, S. 2015, ApJ, 813, 110
Harris, C. R., Millman, K. J., van der Walt, S. J., et al. 2020, Natur, 585, 357
Harris, J., & Zaritsky, D. 2004, AJ, 127, 1531
Harris, J., & Zaritsky, D. 2006, AJ, 131, 2514
Haschke, R., Grebel, E. K., & Duffau, S. 2012, AJ, 144, 107
Hota, S., Subramaniam, A., Nayak, P. K., & Subramanian, S. 2024, AJ, 168, 255
Hunter, J. D. 2007, CSE, 9, 90
Jacyszyn-Dobrzeniecka, A. M., Skowron, D. M., Mróz, P., et al. 2016, AcA, 66, 149
Jacyszyn-Dobrzeniecka, A. M., Skowron, D. M., Mróz, P., et al. 2017, AcA, 67, 1
James, D., Subramanian, S., Omkumar, A. O., et al. 2021, MNRAS, 508, 5854
Jiménez-Arranz, Ó., Romero-Gómez, M., Luri, X., & Masana, E. 2023, A&A, 672, A65
Kallivayalil, N., van der Marel, R. P., Besla, G., Anderson, J., & Alcock, C. 2013, ApJ, 764, 161
Klimentowski, J., Lokas, E. L., Kazantzidis, S., et al. 2007, MNRAS, 378, 353
Loiseau, N., & Bajaja, E. 1981, RMxAA, 6, 55
Muller, E., & Bekki, K. 2007, MNRAS, 381, L11
Muraveva, T., Subramanian, S., Clementini, G., et al. 2018, MNRAS, 473, 3131
Nidever, D. L., Majewski, S. R., Burton, W. B., & Nigra, L. 2010, ApJ, 723, 1618
Nidever, D. L., Majewski, S. R., & Butler Burton, W. 2008, ApJ, 679, 432
Niederhofer, F., Cioni, M. R. L., Rubele, S., et al. 2018, A&A, 613, L8
Niederhofer, F., Cioni, M.-R. L., Rubele, S., et al. 2021, MNRAS, 502, 2859
Oey, M. S., Jones, J. D., Castro, N., et al. 2018, ApJL, 867, L8
Omkumar, A. O., Subramanian, S., Niederhofer, F., et al. 2021, MNRAS, 500, 2757
Piatti, A. E. 2022, MNRAS, 509, 3462
Piatti, A. E. 2021, A&A, 650, A52
Pietrzyński, G., Graczyk, D., Gallenne, A., et al. 2019, Natur, 567, 200
Putman, M. E., Gibson, B. K., Staveley-Smith, L., et al. 1998, Natur, 394, 752
Putman, M. E., Staveley-Smith, L., Freeman, K. C., Gibson, B. K., & Barnes, D. G. 2003, ApJ, 586, 170
Ripepi, V., Cioni, M.-R. L., Moretti, M. I., et al. 2017, MNRAS, 472, 808
Rubele, S., Pastorelli, G., Girardi, L., et al. 2018, MNRAS, 478, 5017
Sakowska, J. D., Nol, N. E. D., Ruiz-Lara, T., et al. 2024, MNRAS, 532, 4272
Saroon, S., & Subramanian, S. 2022, A&A, 666, A103
Stanimirović, S., Staveley-Smith, L., & Jones, P. A. 2004, ApJ, 604, 176
Subramanian, S., & Subramaniam, A. 2012, ApJ, 744, 128
Subramanian, S., & Subramaniam, A. 2015, A&A, 573, A135
Subramanian, S., Rubele, S., Sun, N.-C., et al. 2017, MNRAS, 467, 2980
Tatton, B. L., van Loon, J. T., Cioni, M. R. L., et al. 2021, MNRAS, 504, 2983
van der Marel, R. P., Alves, D. R., Hardy, E., & Suntzeff, N. B. 2002, AJ, 124, 2639
van der Marel, R. P., & Sahlmann, J. 2016, ApJL, 832, L23
Venzmer, M. S., Kerp, J., & Kalberla, P. M. W. 2012, A&A, 547, A12
Virtanen, P., Gommers, R., Oliphant, T. E., et al. 2020, NatMe, 17, 261
Weinberg, M. D. 2000, ApJ, 532, 922
Zaritsky, D., Harris, J., Grebel, E. K., & Thompson, I. B. 2000, ApJL, 534, L53
Zivick, P., Kallivayalil, N., & van der Marel, R. P. 2021, ApJ, 910, 36
Zivick, P., Kallivayalil, N., van der Marel, R. P., et al. 2018, ApJ, 864, 55